catalysts

MDPI

Article

Construction of Bronze TiO_2/Ti_3C_2 MXene/Ag_3PO_4 Ternary Composite Photocatalyst toward High Photocatalytic Performance

Yong Li [1,2,†], Mingqing Zhang [1,2,†], Yanfang Liu [1,2,†], Qinghua Zhao [1,2], Xin Li [1,2], Qianyu Zhou [1,2], Yuanfu Chen [3,*] and Shifeng Wang [1,2,*]

1 Innovation Laboratory of Materials for Energy and Environment Technologies, Institute of Oxygen Supply, Tibet University, Lhasa 850012, China; liyongzzu@163.com (Y.L.); mingqing@utibet.edu.cn (M.Z.); liuyanfang@utibet.edu.cn (Y.L.); zhaoqinghua@utibet.edu.cn (Q.Z.); lixin@utibet.edu.cn (X.L.); zhouqianyu@utibet.edu.cn (Q.Z.)
2 Key Laboratory of Cosmic Rays (Tibet University), Ministry of Education, Lhasa 850012, China
3 School of Electronic Science and Engineering, State Key Laboratory of Electronic Thin Films and Integrated Devices, University of Electronic Science and Technology of China, Chengdu 610054, China
* Correspondence: yfchen@uestc.edu.cn (Y.C.); wsf365@163.com (S.W.)
† These authors contributed equally to this work.

Abstract: Research has demonstrated that the formation of composites of titanium dioxide (TiO_2) with silver phosphate (Ag_3PO_4) through the construction of heterojunctions can expand its light absorption range and suppress the recombination of photogenerated electron–hole pairs, thereby improving the photocatalytic performance. However, this method offers only limited performance improvements, and the composite photocatalysts are costly due to the expensive Ag_3PO_4. In this study, Ti_3C_2 MXene, which has good hydrophilicity and excellent electrical conductivity, is first used to form Schottky junction composites with bronze TiO_2 (TiO_2(B)) via electrostatic self-assembly. Then, Ag_3PO_4 quantum dots were further formed on the surface of the TiO_2(B)/Ti_3C_2 MXene by in situ self-growth, and Ag_3PO_4 formed heterojunctions and Schottky junctions with TiO_2(B) and Ti_3C_2 MXene, respectively. Finally, a ternary composite photocatalyst TiO_2(B)/Ti_3C_2 MXene/Ag_3PO_4 was jointly constructed by these functional junctions. Under the synergistic effect of these functional junctions, the mobility and fast separation performance of photogenerated electron–hole pairs of the composite photocatalyst were significantly improved, the recombination of photogenerated electron–hole pairs was effectively suppressed, and the light absorption performance was enhanced. As a result, the composite photocatalyst exhibited excellent photocatalytic performances.

Keywords: ternary composite photocatalyst; heterojunction; photocatalytic degradation; bronze TiO_2; Ti_3C_2 MXene

check for updates

Citation: Li, Y.; Zhang, M.; Liu, Y.; Zhao, Q.; Li, X.; Zhou, Q.; Chen, Y.; Wang, S. Construction of Bronze TiO_2/Ti_3C_2 MXene/Ag_3PO_4 Ternary Composite Photocatalyst toward High Photocatalytic Performance. *Catalysts* **2022**, *12*, 599. https://doi.org/10.3390/catal12060599

Academic Editors: Ravindranadh Koutavarapu and Malathi Arumugam

Received: 12 May 2022
Accepted: 29 May 2022
Published: 31 May 2022

1. Introduction

The titanium dioxide (TiO_2) photocatalyst has been widely studied as a safe, inexpensive, and environmentally friendly photocatalyst. However, it does not exhibit high photocatalytic performances since it is only active for ultraviolet (UV) light due to its wide forbidden band gap and because the photogenerated electron–hole pairs easily recombine [1–4]. Previous studies have demonstrated that the compositing of TiO_2 and silver phosphate (Ag_3PO_4) via the construction of heterojunctions can expand its light absorption range and suppress the recombination of photogenerated electron–hole pairs, thereby improving the photocatalytic performance. However, such a performance improvement is limited, and the composite catalysts are costly due to the expensive Ag_3PO_4 [5–8]. Ti_3C_2 MXene is a new two-dimensional material with good hydrophilicity and excellent electrical conductivity. It can be used as a co-catalyst with other semiconductors to form Schottky junctions, which can not only effectively expand the light absorption range but also

promote the rapid separation of photogenerated electron–hole pairs, thus enhancing the photocatalytic performances of the composite photocatalysts [9–12].

To obtain high-performance and low-cost photocatalysts, TiO_2(B)/Ti_3C_2 MXene/Ag_3PO_4 ternary composite photocatalysts were constructed in this study. First, a TiO_2(B)/Ti_3C_2 MXene composite was constructed by electrostatic self-assembly of strip-like TiO_2(B) and lamellar Ti_3C_2 MXene, and then Ag_3PO_4 quantum dots were formed on the surface of the TiO_2(B)/Ti_3C_2 MXene by in situ growth, thereby forming the TiO_2/Ti_3C_2 MXene/Ag_3PO_4 ternary composite photocatalyst. The composite photocatalyst exhibited excellent photocatalytic performances, which first increased and then decreased with the increase in the content of the co-catalyst Ti_3C_2 MXene. The composite photocatalyst reached the best performance when the content of Ti_3C_2 MXene was 20% of the mass of TiO_2(B). Compared with the common TiO_2 phases (anatase, brookite, and rutile), bronze TiO_2 has a good electrical conductivity and a loose, porous structure, which facilitates the rapid migration of carriers and the formation of reaction sites in heterojunction photocatalysts, ultimately enhancing the performances of composite photocatalysts. Therefore, bronze TiO_2 was used in this study as a component of the composite photocatalyst [13–16].

2. Results and Discussion

As shown in Figure 1a, the standard PDF cards of Ag_3PO_4, TiO_2(B), and Ti_3AlC_2 were JCPDS#06-0505, JCPDS#35-0088, and JCPDS#015-3266, respectively. The diffraction pattern of the Ti_3C_2 MXene demonstrated that, after HF etching, the strongest diffraction peak of Ti_3AlC_2 was at $2\theta = 28.99^\circ$, corresponding to the (104) crystal plane disappearing, while the diffraction peaks at $2\theta = 9.52^\circ$ and 19.12° corresponding to the (002) and (004) crystal planes, respectively, were enhanced, and their positions shifted towards smaller diffraction angles. Referring to the literature [17–20], the characteristics of the above diffraction peaks indicated that the Al atomic layer of Ti_3AlC_2 was successfully removed via etching to obtain the Ti_3C_2 MXene in this study. A comparison of the XRD (X-ray diffraction) patterns of the TiO_2(B)/20%Ti_3C_2, Ti_3C_2 MXene, and TiO_2(B) revealed that the diffraction peaks of the TiO_2(B)/20%Ti_3C_2 spectrum were mainly those of TiO_2(B), which appeared weakly and were only observed at $2\theta = 9.14^\circ$, corresponding to the (002) crystal plane of the Ti_3C_2 MXene. In addition, compared with that of the TiO_2(B), the half-peak width of the diffraction peak of the TiO_2(B)/20%Ti_3C_2 spectrum increased, which may have been due to the low content of the Ti_3C_2 MXene and the relatively weak diffraction peaks. Figure 1b shows that the diffraction pattern of the ternary composite was mainly composed of diffraction peaks corresponding to Ag_3PO_4, while those corresponding to the Ti_3C_2 MXene and TiO_2(B) were not observed, which was mainly because Ag_3PO_4 had good crystallinity and exhibited strong diffraction compared to the Ti_3C_2 MXene and TiO_2(B).

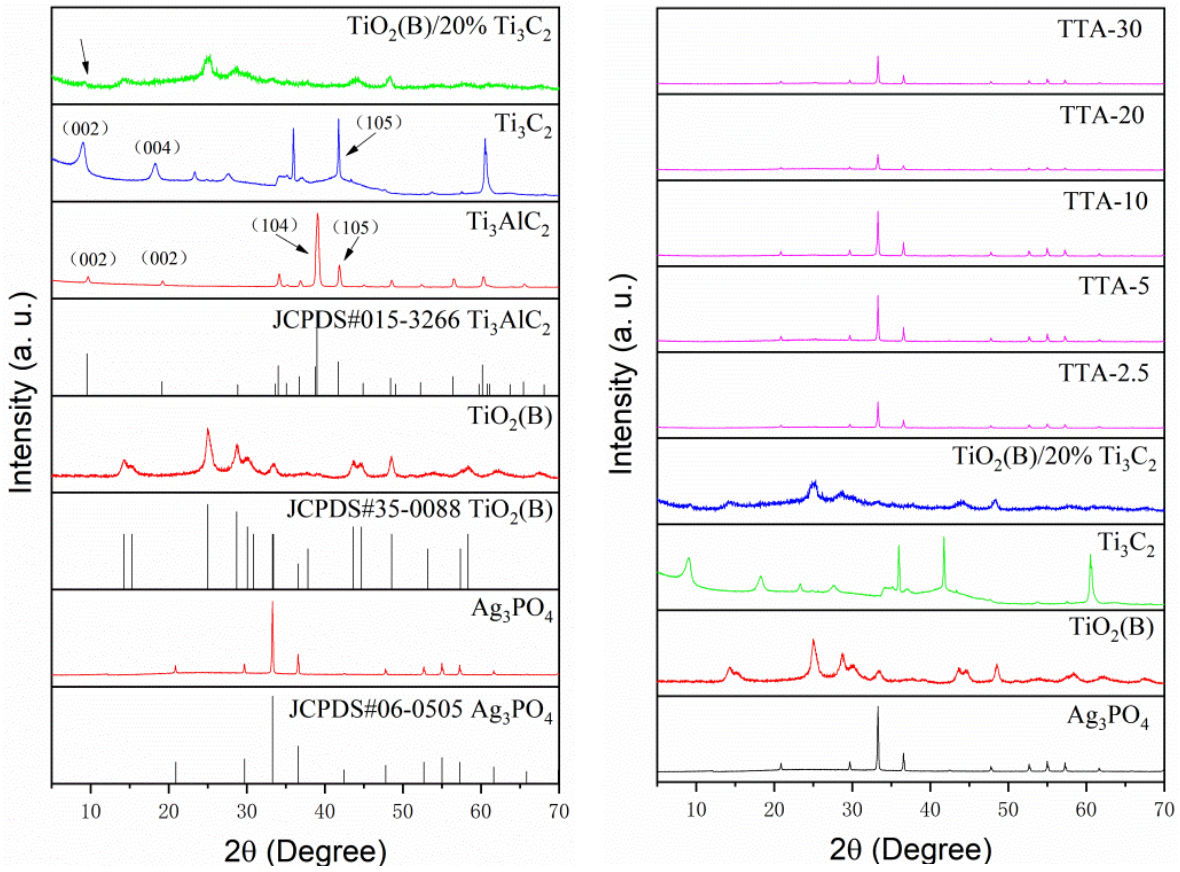

Figure 1. (**a**) XRD diffraction patterns of Ag_3PO_4, TiO_2(B), Ti_3AlC_2, Ti_3C_2 and TiO_2(B)/20%Ti_3C_2; (**b**) XRD diffraction patterns of TTA-2.5, TTA-5, TTA-10, TTA-20 and TTA-30.

Figure 2a shows the SEM (scanning electron microscope) image of the Ti_3C_2 MXene prepared from Ti_3AlC_2. Since the Al atomic layer in the Ti_3AlC_2 was removed by etching, the Ti_3C_2 MXene had an accordion-like morphology, which is typical of Ti_3C_2 MXene. Figure 2b shows the SEM image of the experimentally prepared bronze TiO_2, which had a strip-like morphology. Figure 2c shows the SEM image of the TiO_2(B)/Ti_3C_2 MXene/Ag_3PO_4 ternary composite, showing that the Ti_3C_2 MXene was closely combined with the TiO_2(B), with a large number of fine Ag_3PO_4 particles distributed on their surfaces, which are shown more clearly in the TEM(Transmission Electron Microscope) images in Figure 2d,f. Figure 2e,g show the HRTEM (High Resolution Transmission Electron Microscope) images, from which we can observe the lattices of Ag_3PO_4 (211), bronze TiO_2 (110), and Ti_3C_2 (105) as well as heterojunctions formed in the overlapping regions of these lattices. Figure 2h shows the mapping diagram of the elements in the composite, revealing that the composite contained five elements (Ti, O, Ag, P, and C), the distributions of which were consistent with the above phase and morphological analysis.

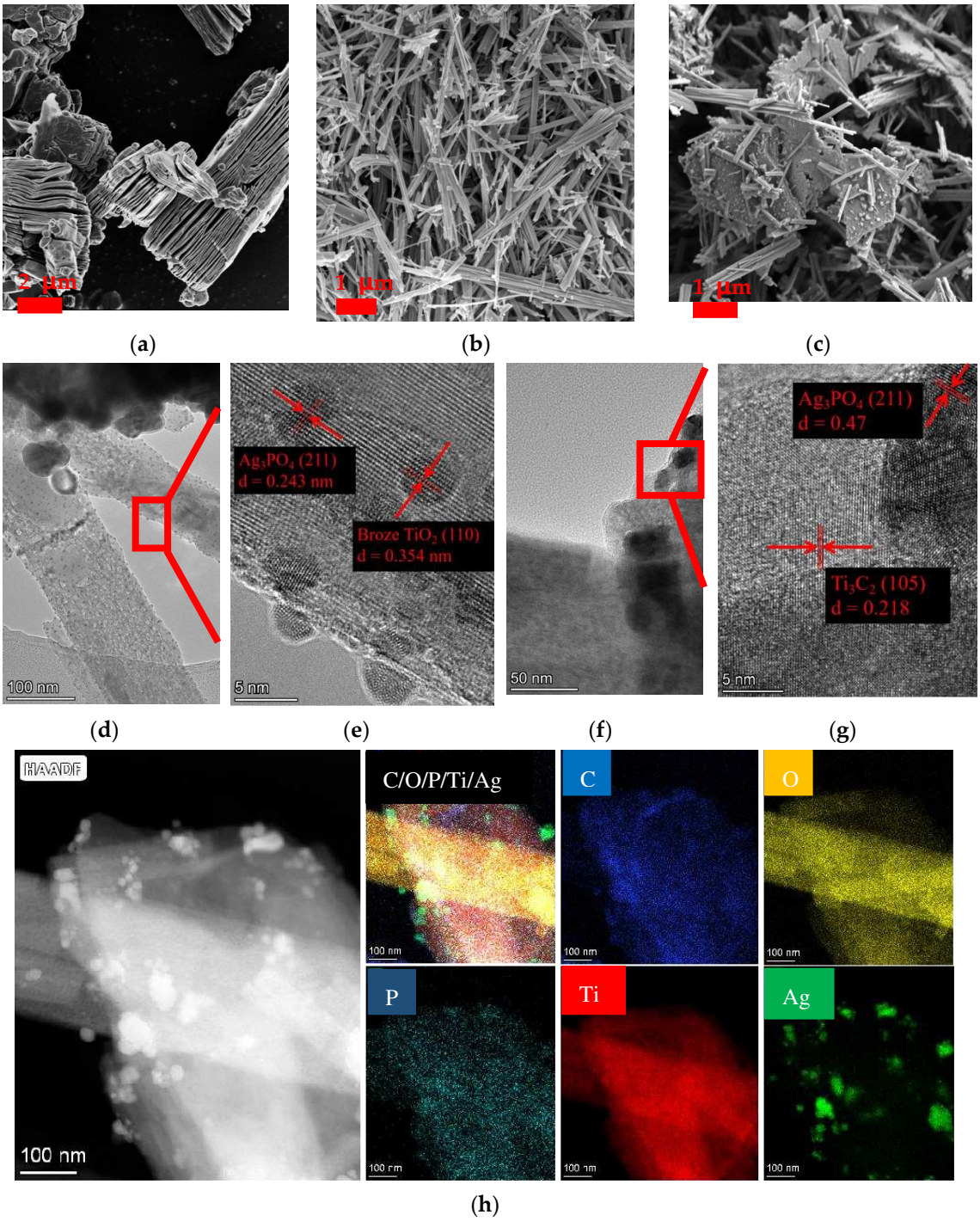

Figure 2. (**a**) SEM of Ti_3C_2 MXene; (**b**) SEM of TiO_2(B); (**c**) SEM of TiO_2(B)/20%Ti_3C_2 MXene/Ag_3PO_4; (**d**,**f**) TEM of TiO_2(B)/20%Ti_3C_2 MXene/Ag_3PO_4; (**e**,**g**) HRTEM of TiO_2(B)/20%Ti_3C_2 MXene/Ag_3PO_4; (**h**) mapping and HAADF (high angle annular dark field image) of samples.

Figure 3a shows the degradation curves of the samples. The photocatalytic performance of the TiO_2(B)/Ti_3C_2 MXene/Ag_3PO_4 composite was significantly higher than those of the TiO_2(B), Ag_3PO_4 and TiO_2(B)/20%Ti_3C_2 MXene and is significantly higher than that of photocatalyst P_{25} sold in the market. The photocatalytic performance of the TiO_2(B)/Ti_3C_2 MXene/Ag_3PO_4 composite first increased with the increase in the content of the Ti_3C_2 MXene and reached the highest value when the content was increased to 20%, beyond which further increases and lowered the photocatalytic performance of the composite instead. Figure 3b shows a linear fit of the degradation kinetics of the sam-

ples. According to the Langmuir–Hinshelwood model, the degradation reaction can be considered to be a first-order reaction at low RhB concentrations, and thus, the fitting of the degradation kinetics can be simplified to a linear case. The degradation reaction in this experiment satisfied the apparent first-order reaction rate equation $\ln(C/C_0) = -k \cdot t$, where k is the apparent first-order reaction rate constant. Thus, $\ln(C/C_0)$ is a function of the irradiation time t. The k values of the TiO_2(B), TiO_2(B)/20%Ti_3C_2 MXene, Ag_3PO_4 and P_{25} were low, with values of 0.008, 0.011, 0.085 and 0.04 min^{-1}, respectively, while the k value corresponding to TTA(TiO_2(B)/Ti_3C_2 MXene/Ag_3PO_4) was significantly higher, which gradually increased from $k_{TTA\text{-}2.5}$ = 0.182 min^{-1} to the maximum $k_{TTA\text{-}20}$ = 0.345 min^{-1} and then decreased to $k_{TTA\text{-}30}$ = 0.241 min^{-1}.

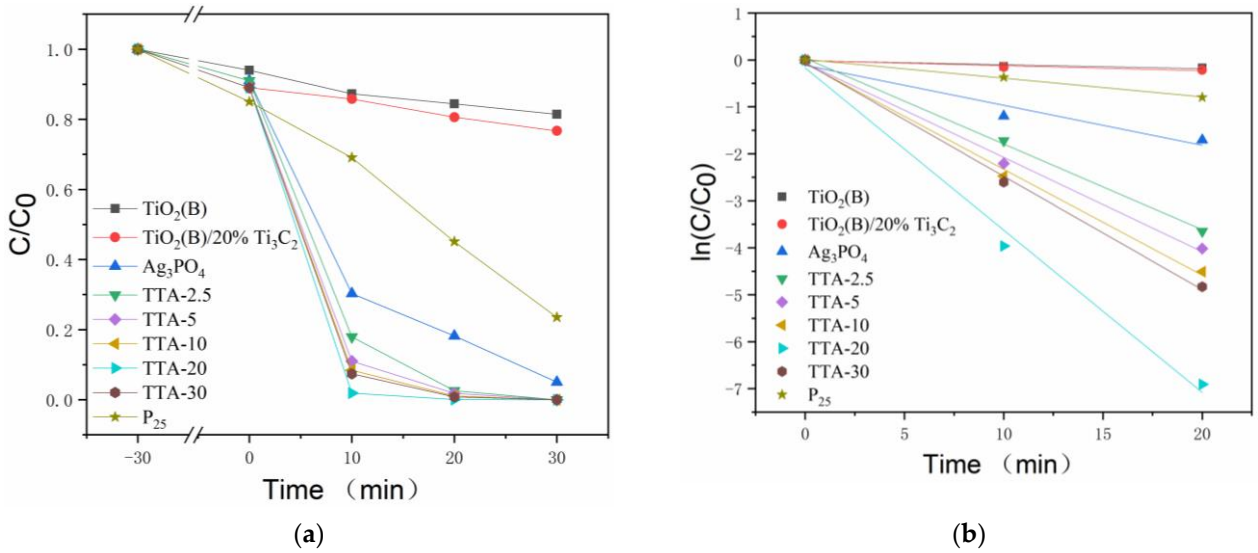

Figure 3. (**a**) Photocatalytic degradation curves; (**b**) linear fittings of degrading kinetics under different catalytic conditions.

Figure 4 shows the UV-Vis absorption spectra of the samples. Compared with TiO_2(B), the visible light absorption capacity was clearly improved after forming a composite of TiO_2(B) and Ti_3C_2 MXene, and the light absorption performance of sample TTA-20 obtained by further incorporating Ag_3PO_4 was even higher. The band gaps of the Ti_3C_2, TiO_2(B), TiO_2(B)/20%Ti_3C_2 MXene, and TTA-20 were calculated to be 1.67, 3.14, 3.23, and 3.32 eV, respectively, based on the Tauc plot. These results confirmed the band gap reduction by the formation of the composite, which is an important reason for the improved light absorption performances of the composite materials.

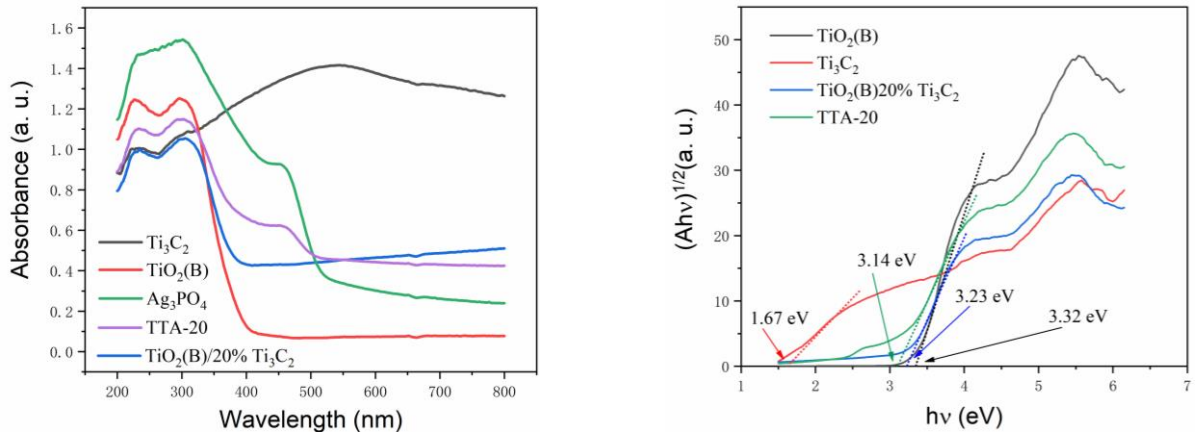

(**a**) (**b**)

Figure 4. (**a**) Ultraviolet-visible (UV-Vis) absorption spectra and (**b**) band gaps of samples.

As shown in Figure 5, the fluorescence emission spectra as well as the transient photocurrent response and electrochemical impedance Nyquist plots of the samples were obtained to analyze the influence of the formation of composites on the recombination and migration of photogenerated electron–hole pairs in the samples. Figure 5a shows that the fluorescence of the TiO_2(B)/20%Ti_3C_2 MXene was significantly weaker than that of the TiO_2(B), and the fluorescence of TTA-20 (TiO_2(B)/20%Ti_3C_2 MXene/Ag_3PO_4) was the weakest. This was because the highly conductive Ti_3C_2 MXene was composited with TiO_2(B) to form Schottky junctions on the contact surface, which caused the fast migration of photogenerated electrons to the Ti_3C_2 MXene, achieving rapid separation of photogenerated electron–hole pairs and suppressing the recombination. By forming the Ti_3C_2 MXene and TiO_2(B) composite, Ag_3PO_4 quantum dots were introduced on the surfaces of the Ti_3C_2 MXene and TiO_2(B) by in situ self-growth, the Ag_3PO_4 and Ti_3C_2 MXene formed Schottky junctions, and the Ag_3PO_4 and TiO_2(B) formed heterojunctions. These junctions created a synergistic effect with the Schottky junctions formed by the Ti_3C_2 MXene and TiO_2(B), further promoting the rapid migration and separation of photogenerated electrons and greatly suppressing the recombination of photogenerated electron–hole pairs. Figure 5b shows the transient photocurrent responses of the samples. The photocurrents of the samples were enhanced by compositing. The photocurrent of TTA-20 was the strongest, followed by those of the TiO_2(B)/20%Ti_3C_2 MXene, Ag_3PO_4, and TiO_2(B), in that order. The photocurrent enhancement pattern was consistent with the fluorescence weakening pattern, and the photocurrent enhancement also indicated that the recombination of photogenerated electron–hole pairs was effectively suppressed. Thus, Figure 5b further confirms the results and analysis of Figure 5a. Figure 5c shows the Nyquist plot of the electrochemical impedances of the samples. In general, the smaller the curvature radius of the curve is, the greater the electron mobility of the sample is. The mobility was significantly enhanced by forming the composite. The electron mobility of TTA-20 was the largest, followed by that of the TiO_2(B)/20%Ti_3C_2 MXene, and both were larger than those of the TiO_2(B) and Ag_3PO_4.

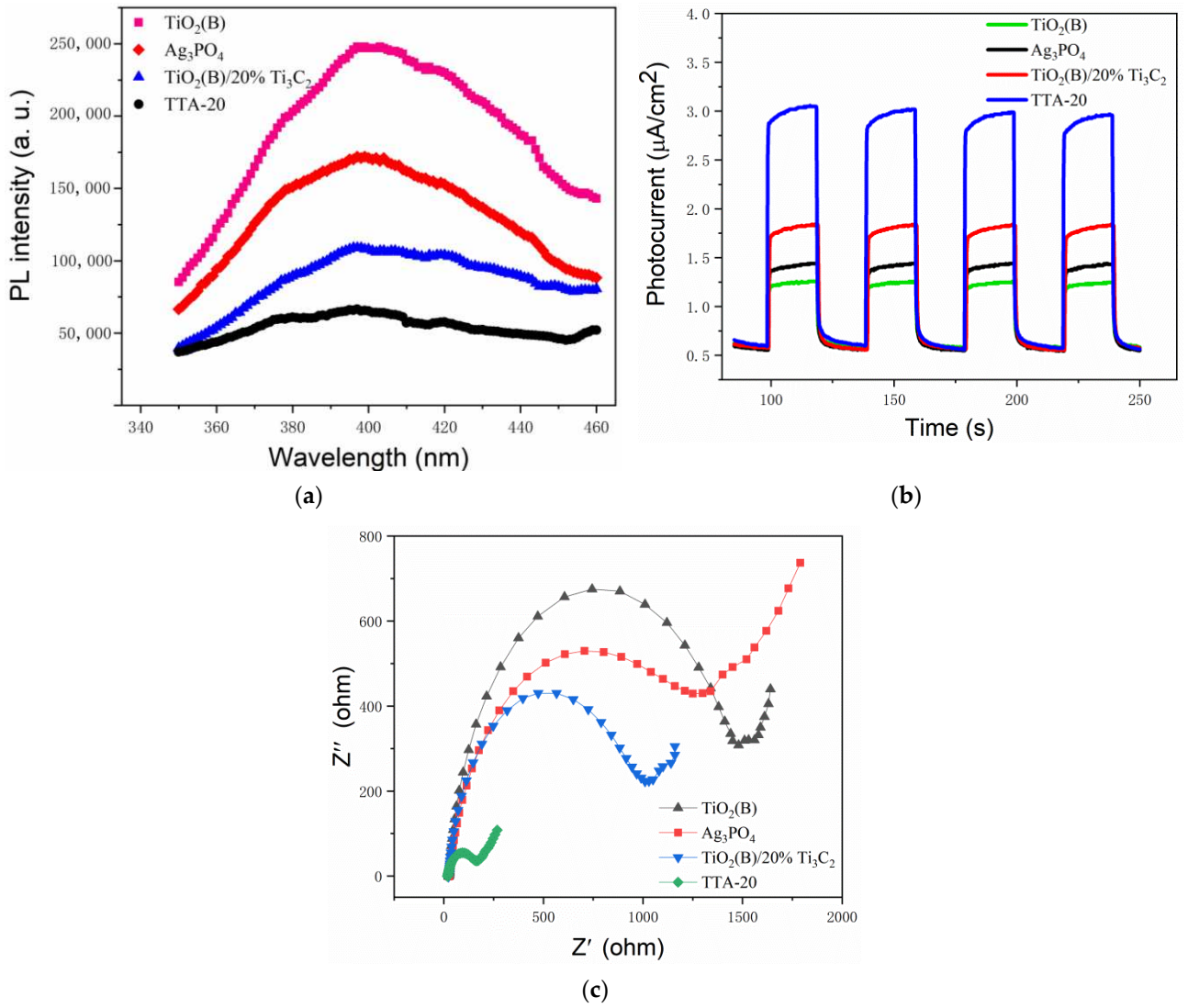

Figure 5. (**a**) Photoluminescence (PL) spectra; (**b**) transient photocurrent responses; (**c**) electrochemical impedance Nyquist.

3. Materials and Experiments

3.1. Preparation of Materials and Samples

The following reagents were used: Rhodamine B (RhB, $C_{28}H_{31}ClN_2O_3$) (Solarbio, Beijing, China); titanium aluminum carbide (Ti_3AlC_2) (Xianfeng Nanomaterials, Nanjing, China); disodium hydrogen phosphate 12-water ($Na_2HPO_4{\cdot}12H_2O$, Jinshan Chemical Reagent, Chengdu, China); silver nitrate ($AgNO_3$) (Sinopharm Chemical Reagent, Shanghai, China); and sodium hydroxide (NaOH), hydrofluoric acid (HF), and nano-TiO_2 (Aladdin Industrial, Shanghai, China). The deionized (DI) water used for the experiments was prepared in our laboratory. All reagents were of analytical grade and were used without further purification.

Ti_3C_2 MXene was prepared from Ti_3AlC_2 by HF etching as follows. An appropriate amount of 40% (mass fraction) Ti_3AlC_2 was slowly added to the HF acid solution at a ratio of 1 g/20 mL and stirred at room temperature for 24 h. The prepared product was separated by centrifugation at 4000 rpm and rinsed repeatedly with DI water to near neutrality.

The preparation of TiO_2(B) was as follows. A 10 M NaOH aqueous solution was prepared. Then, raw TiO_2 was added, stirred well, poured into a hydrothermal reactor, and heated up to 200 °C in a blast drying oven and held for 24 h. Next, the reaction product was removed, rinsed with a large amount of DI water to near neutrality, soaked with 0.1 M

dilute hydrochloric acid for 72 h, rinsed again with a large amount of DI water to near neutrality, dried at 60 °C for 10 h, and finally calcined in a muffle furnace at 500 °C for 2 h to obtain TiO_2(B).

The TiO_2(B)/Ti_3C_2 MXene/Ag_3PO_4 ternary composite was prepared as follows. About 100 mg of TiO_2(B) and 20 mg of Ti_3C_2 MXene were added to DI water and sonicated for 4 h to allow the formation of a composite of TiO_2(B) and Ti_3C_2 MXene by electrostatic self-assembly, which was followed by drying in a vacuum drying oven to obtain the TiO_2(B)/20%Ti_3C_2 MXene composite. $Na_2HPO_4{\cdot}12H_2O$ and TiO_2(B)/20%Ti_3C_2 MXene were added to DI water at a molar ratio of 0.8:1 (note that the number of moles of TiO_2(B)/20%Ti_3C_2 MXene was the sum of the numbers of moles of the two components) and mixed well. A solution was prepared using $AgNO_3$ in a molar ratio of 3:1 with $Na_2HPO_4{\cdot}12H_2O$, and then the solution was slowly added dropwise using a syringe to the mixture of $Na_2HPO_4{\cdot}12H_2O$ and TiO_2(B)/20%Ti_3C_2 MXene. The mixture was stirred continuously to form Ag_3PO_4 quantum dots on the surface of the TiO_2(B)/20%Ti_3C_2 MXene via in situ self-growth. The product was rinsed with DI water and dried in the vacuum drying oven to obtain TiO_2(B)/20%Ti_3C_2 MXene/Ag_3PO_4, which was labeled as TTA-20. The preparation flow chart is shown in Figure 6. Using the same method, TiO_2(B)/2.5%Ti_3C_2 MXene/Ag_3PO_4, TiO_2(B)/5%Ti_3C_2 MXene/Ag_3PO_4, TiO_2(B)/10%Ti_3C_2 MXene/Ag_3PO_4, and TiO_2(B)/30%Ti_3C_2 MXene/Ag_3PO_4 were prepared and labeled as TTA-2.5, TTA-5, TTA-10, and TTA-30, respectively.

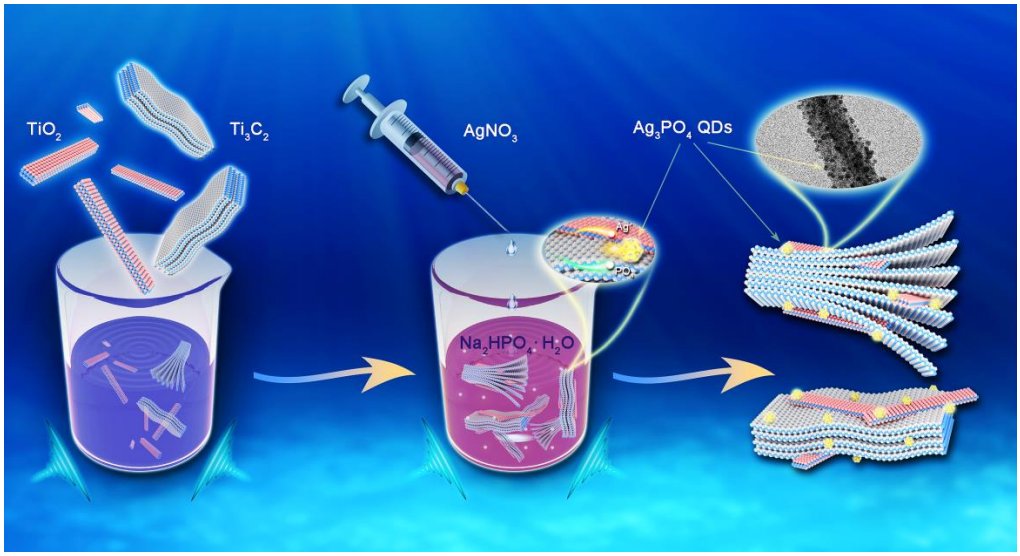

Figure 6. Preparation flow chart of TiO_2(B)/Ti_3C_2 MXene/Ag_3PO_4 ternary composite.

3.2. Analytical Tests

An X-ray powder diffraction (XRD, BRUCKER D8 ADVANCE, Bruker, Bremen, Germany) was used to test and analyze the phases of the samples using the following test parameters: Cu target, wide-angle diffraction, scan range of 5°–70°, scan rate of 10°/min, test wavelength of 1.5406 Å, tube voltage of 40 kV, and tube current of 40 mA. Field-emission scanning electron microscopy (FE-SEM, Gemini SEM 300, Zeiss, Oberkochen, Germany) was used to characterize the morphologies and structures of the samples at an operating voltage of 3 kV. Field-emission transmission electron microscopy (FEI Talos F200X, FEI, Hillsboro, OR, USA), with a maximum magnification of 1.1 million times and a limit resolution of 0.12 nm, was used to observe and analyze the morphologies and structures of the samples at an operating voltage of 200 kV. An ultraviolet–visible (UV-Vis) spectrophotometer (UV-3600, Shimadzu company, Kyoto, Japan), with a test range of 200–2500 nm, was used to test the photocatalytic degradation of RhB and obtain the UV-Vis absorption spectra of the samples. An electrochemical workstation (CHI-760E, Shanghai

Chenhua Instrument, Shanghai, China) was used to test the photocurrents and impedances of the samples.

Two liters of 20 mg/L RhB solution were prepared, and 100 mL was taken for each experiment, added to 20 mg of the sample, and sonicated for 30 min. Then, this mixture was placed under a light source with an intensity of 600 W/m^2 (at the liquid surface) in a solar simulator (Solar-500Q, Newbit, Beijing, China) to start the photocatalytic degradation experiment, which lasted for 60 min. During the experiment, 5 mL of liquid was taken from the mixture every 10 min and subjected to centrifugation at 10,000 rpm for 10 min. After centrifugation, the supernatant was taken and its absorbance A_n was measured by the UV-Vis spectrophotometer. There was a direct proportionality relation between the solution concentration C_n and A_n, $C_n/C_0 = A_n/A_0$, where C_0 was the concentration of 20 mg/L of the RhB solution, and A_0 was the absorbance of the 20 mg/L RhB solution.

4. Conclusions

In this study, the TiO_2(B)/Ti_3C_2 MXene Schottky junction composite was first prepared by electrostatic self-assembly, and then Ag_3PO_4 quantum dots were generated on the surface of the TiO_2(B)/Ti_3C_2 MXene by in situ self-growth, thereby forming Ag_3PO_4/TiO_2(B) heterojunctions and Ag_3PO_4/Ti_3C_2 MXene Schottky junctions. Through the successful construction and synergy of these functional junctions (As shown in Figure 7), the light absorption capacity of the composite photocatalyst was greatly enhanced, and the recombination of photogenerated electron–hole pairs was effectively suppressed, thus substantially improving the photocatalytic degradation performance of the composite photocatalyst. It was further found that the photocatalytic performance of the TiO_2(B)/Ti_3C_2 MXene/Ag_3PO_4 composite increased with the increase in the Ti_3C_2 MXene content, and it reached the maximum when the Ti_3C_2 MXene content increased to 20%, beyond which the photocatalytic performance of the composite decreased as the Ti_3C_2 MXene content continued to increase.

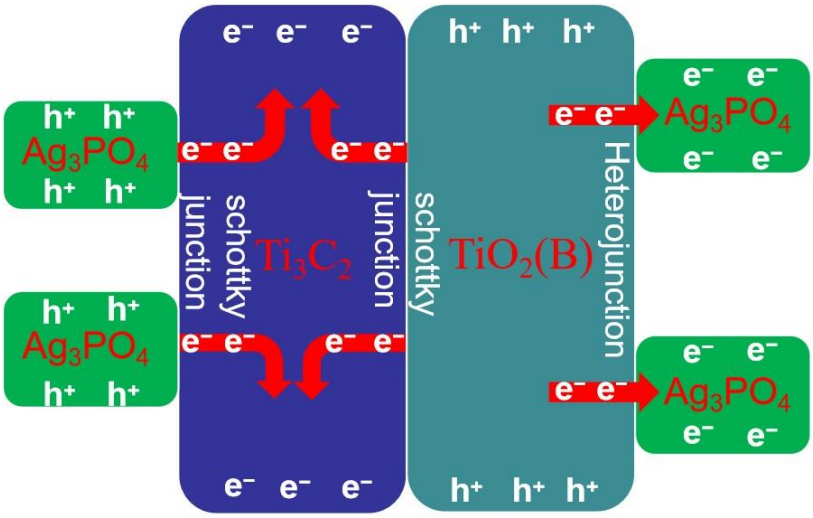

Figure 7. Mechanism of enhanced photocatalytic properties.

Author Contributions: Conceptualization, methodology, S.W. and Y.C.; software, Y.L. (Yong Li); validation, Y.L. (Yong Li) and Y.L. (Yanfang Liu); formal analysis, Y.L. (Yong Li) and M.Z.; investigation, Y.L. (Yong Li), Y.L. (Yanfang Liu) and M.Z.; resources, S.W. and Y.C.; data curation, S.W. writing—original draft preparation, Y.L. (Yong Li), M.Z. and X.L.; writing—review and editing, Y.L. (Yong Li), M.Z. and Y.L. (Yanfang Liu); visualization, Q.Z. (Qinghua Zhao) and Q.Z. (Qianyu Zhou); project administration, Y.L. (Yong Li).; funding acquisition, Y.L. (Yong Li) and S.W. All authors have read and agreed to the published version of the manuscript.

Funding: The National Natural Science Foundation of China (Grant No.: 52062045), Central Government Funds for Local Scientific and Technological Development (Grant No.: XZ202101YD0019C

and XZ202201YD0026C), Natural Science Foundation of Tibet Autonomous Region (Grant No. XZ202101ZR0121G), and Everest Discipline Construction Project of Tibet University (Grant No.: ZF22004002).

Data Availability Statement: The data presented in this study are available on request from the corresponding author.

Conflicts of Interest: The authors declare no conflict of interest.

References

1. Zhang, W.; He, H.; Li, H.; Duan, L.; Zu, L.; Zhai, Y.; Li, W.; Wang, L.; Fu, H.; Zhao, D. Visible-light responsive TiO_2-based materials for efficient solar energy utilization. *Adv. Energy Mater.* **2021**, *11*, 2003303. [CrossRef]
2. Lu, Y.; Liu, X.-L.; He, L.; Zhang, Y.-X.; Hu, Z.-Y.; Tian, G.; Cheng, X.; Wu, S.-M.; Li, Y.-Z.; Yang, X.-H. Spatial heterojunction in nanostructured TiO2 and its cascade effect for efficient photocatalysis. *Nano Lett.* **2020**, *20*, 3122–3129. [CrossRef] [PubMed]
3. Paumo, H.K.; Dalhatou, S.; Katata-Seru, L.M.; Kamdem, B.P.; Tijani, J.O.; Vishwanathan, V.; Kane, A.; Bahadur, I. TiO2 assisted photocatalysts for degradation of emerging organic pollutants in water and wastewater. *J. Mol. Liq.* **2021**, *331*, 115458. [CrossRef]
4. Lettieri, S.; Pavone, M.; Fioravanti, A.; Santamaria Amato, L.; Maddalena, P. Charge carrier processes and optical properties in TiO_2 and TiO_2-based heterojunction photocatalysts: A review. *Materials* **2021**, *14*, 1645. [CrossRef] [PubMed]
5. Li, Y.; Liu, Y.; Zhang, M.; Zhou, Q.; Li, X.; Chen, T.; Wang, S. Preparation of Ag_3PO_4/TiO_2(B) heterojunction nanobelt with extended light response and enhanced photocatalytic performance. *Molecules* **2021**, *26*, 6987. [CrossRef]
6. Liu, B.; Xue, Y.; Zhang, J.; Han, B.; Zhang, J.; Suo, X.; Mu, L.; Shi, H. Visible-light-driven TiO_2/Ag_3PO_4 heterostructures with enhanced antifungal activity against agricultural pathogenic fungi Fusarium graminearum and mechanism insight. *Environ. Sci. Nano* **2017**, *4*, 255–264. [CrossRef]
7. Liu, C.-F.; Perng, T.-P. Fabrication and band structure of Ag3PO4–TiO2 heterojunction with enhanced photocatalytic hydrogen evolution. *Int. J. Hydrogen Energy* **2020**, *45*, 149–159. [CrossRef]
8. Qiu, B.; Mao, Y.; Xiao, X.; Zhang, M.; Liu, X. Study on the photocatalytic performance of TiO2 composited with Ag3PO4 based on biological template. *Sol. Energy* **2021**, *220*, 63–69. [CrossRef]
9. Hieu, V.Q.; Phung, T.K.; Nguyen, T.-Q.; Khan, A.; Doan, V.D.; Tran, V.A.; Le, V.T. Photocatalytic degradation of methyl orange dye by Ti_3C_2–TiO_2 heterojunction under solar light. *Chemosphere* **2021**, *276*, 130154. [CrossRef] [PubMed]
10. Zhang, H.; Li, M.; Wang, W.; Zhang, G.; Tang, Q.; Cao, J. Designing 3D porous BiOI/Ti3C2 nanocomposite as a superior coating photocatalyst for photodegradation RhB and photoreduction Cr (VI). *Sep. Purif. Technol.* **2021**, *272*, 118911. [CrossRef]
11. Liu, W.; Sun, M.; Ding, Z.; Gao, B.; Ding, W. Ti3C2 MXene embellished g-C3N4 nanosheets for improving photocatalytic redox capacity. *J. Alloys Compd.* **2021**, *877*, 160223. [CrossRef]
12. Li, Y.; Liu, Y.; Xing, D.; Wang, J.; Zheng, L.; Wang, Z.; Wang, P.; Zheng, Z.; Cheng, H.; Dai, Y.; et al. 2D/2D heterostructure of ultrathin BiVO4/Ti3C2 nanosheets for photocatalytic overall Water splitting. *Appl. Catal. B* **2021**, *285*, 119855. [CrossRef]
13. VahidMohammadi, A.; Rosen, J.; Gogotsi, Y. The world of two-dimensional carbides and nitrides (MXenes). *Science* **2021**, *372*, 1581. [CrossRef] [PubMed]
14. Xie, F.; Zhu, J.; Li, Y.; Shen, D.; Abate, A.; Wei, M. TiO2-B as an electron transporting material for highly efficient perovskite solar cells. *J. Power Sources* **2019**, *415*, 8–14. [CrossRef]
15. Di, T.; Zhang, J.; Cheng, B.; Yu, J.; Xu, J. Hierarchically nanostructured porous TiO2(B) with superior photocatalytic CO_2 reduction activity. *Sci. China Chem.* **2018**, *61*, 344–350. [CrossRef]
16. Hossain, M.K.; Koirala, A.R.; Akhtar, U.S.; Song, M.K.; Yoon, K.B. First Synthesis of Highly Crystalline, Hexagonally Ordered, Uniformly Mesoporous TiO2–B and Its Optical and Photocatalytic Properties. *Chem. Mater.* **2015**, *27*, 6550–6557. [CrossRef]
17. Li, Z.; Huang, W.; Liu, J.; Lv, K.; Li, Q. Embedding CdS@Au into Ultrathin $Ti_{3-x}C_2T_y$ to Build Dual Schottky Barriers for Photocatalytic H_2 Production. *ACS. Catal.* **2021**, *11*, 8510–8520. [CrossRef]
18. Huang, K.; Li, C.; Wang, L.; Wang, W.; Meng, X. Layered Ti3C2 MXene and silver co-modified g-C3N4 with enhanced visible light-driven photocatalytic activity. *Chem. Eng. J.* **2021**, *425*, 131493. [CrossRef]
19. Chen, Y.; Li, X.; Cai, G.; Li, M.; Tang, D. In situ formation of (0 0 1)TiO_2/Ti_3C_2 heterojunctions for enhanced photoelectrochemical detection of dopamine. *Electrochem. Commun.* **2021**, *125*, 106987. [CrossRef]
20. Cao, Z.; Su, J.; Li, Y.; Li, J.; Wang, Z.; Li, M.; Fan, B.; Shao, G.; Wang, H.; Xu, H. High-energy ball milling assisted one-step preparation of g-C3N4/TiO2@Ti3C2 composites for effective visible light degradation of pollutants—ScienceDirect. *J. Alloys Compd.* **2021**, *889*, 161771. [CrossRef]